Geochemical Perspectives Letters

Sr-Nd-Pb isotopes of fluids in diamond record two-stage modification of the continental lithosphere

Y. Weiss[1*], J.M. Koornneef[2], G.R. Davies[2]

OPEN ACCESS

https://doi.org/10.7185/geochemlet.2329

Abstract

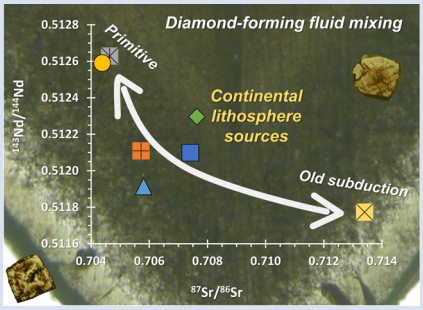

High-density fluid (HDF) microinclusions in diamonds allow direct investigation of deep carbon- and water-rich fluids that influence the properties of Earth's mantle. Identifying the sources and evolution of such fluids in the context of different potential mantle reservoirs is difficult due to the limited radiogenic isotope data. Here, we report Sr-Nd-Pb isotope compositions of silicic to low-Mg carbonatitic HDFs in a suite of diamonds from a single source in Canada. Relationships between isotopes and trace element compositions indicate the contribution of two distinct sources within the continental lithosphere: one with relatively primitive isotopic compositions characterised by εNd of −0.2, $^{87}Sr/^{86}Sr$ of 0.7044 and $^{206}Pb/^{204}Pb$ of 17.52, and another with more unradiogenic εNd < −16 and radiogenic $^{87}Sr/^{86}Sr$ and $^{206}Pb/^{204}Pb$ > 0.713 and 18.3, respectively. We suggest that the latter reflects an old metasomatic event in the continental lithosphere involving fluid addition from a subducting slab, most probably in the Paleoproterozoic. HDFs formed and their host diamonds crystallised in a more recent metasomatic event, indicated by the unaggregated nitrogen of the diamonds, where fluids from both sources mixed. HDFs from Canada, Botswana, and Congo have comparable isotope-trace element relationships, suggesting contributions of similar sources in distinct lithospheric provinces worldwide.

Received 25 April 2022 | Accepted 30 August 2023 | Published 20 September 2023

Introduction

Carbon- and water-rich fluids involved in large-scale tectonic processes carry incompatible element-enriched chemical fingerprints, which are common in metasomatised mantle-derived samples (*e.g.*, Dawson, 1984; Turner *et al.*, 2021). Diamonds are a primary target for studying mantle metasomatic processes, as they form during fluid-rock interaction and often encapsulate ambient minerals and high-density fluids (HDFs; either melt or supercritical fluid). The most common HDFs are found as microinclusions in 'fibrous diamonds' (a fast-growing form of diamond that is usually translucent or opaque with cuboid faces; see Graphical Abstract), which vary in composition between four major types: hydrous-silicic, rich in Si, Al, K and H_2O; low-Mg carbonatitic and high-Mg carbonatitic, both rich in Ca, Mg, Fe, K and CO_2; and hydrous-saline, rich in Cl, K, Na and H_2O (Weiss *et al.*, 2022a). These HDFs provide the opportunity to directly examine the nature of carbon- and water-rich media in the deep Earth and constrain their varying origins (*e.g.*, Smith *et al.*, 2012; Klein-BenDavid *et al.*, 2014; Kempe *et al.*, 2021).

Radiogenic isotopes preserve their signature during mantle processes such as melting and immiscible separation, and are therefore an important tool in tracing mantle sources. Available HDFs Sr isotope data range between 0.703 to 0.723, indicating sources ranging from 'depleted' oceanic mantle to old continental lithosphere (Akagi and Masuda, 1988; Klein-BenDavid *et al.*, 2010, 2014; Smith *et al.*, 2012; Weiss *et al.*, 2015). To date, only a handful of diamond HDFs have been analysed for their Nd and Pb isotope compositions (n = 5 and 3, respectively; Klein-BenDavid *et al.*, 2010, 2014), which hinders unambiguous evaluation of possible mantle sources or recycled surface materials in metasomatic events.

Here, we combine major, trace element and Sr-Nd-Pb isotope compositions of a suite of 7 HDF-bearing fibrous diamonds from Canada to constrain their petrogenesis. Together with the available isotopic data of similar HDF types in diamonds from different lithospheric provinces, we investigate possible HDF origin in the context of large-scale mantle reservoirs and processes, which control the spectrum of HDF compositions and the long-term evolution of the deep carbon cycle.

Samples and Methods

Seven fibrous diamonds from a single source in Canada (exact origin is unknown; see Supplementary Information, Sample Description) were cut by laser to create ~500 µm slabs, polished on both sides, and analysed for their nitrogen characteristics and microinclusion compositions. FTIR (Fourier-transform infrared) spectroscopy establishes they carry 850 to 1250 ppm nitrogen and all exclusively exhibit absorption due to nitrogen in A-centers (a neighbouring pair of substitutional N atoms; pure Type IaA

1. The Freddy and Nadine Herrmann Institute of Earth Sciences, The Hebrew University of Jerusalem, Jerusalem 91904, Israel
2. Vrije Universiteit Amsterdam, Faculty of Science, De Boelelaan 1085, 1081 HV Amsterdam, The Netherlands
* Corresponding author (email: yakov.weiss@mail.huji.ac.il)

spectrum). Major element compositions were determined by EPMA (Electron probe micro-analysis, Kempe *et al.*, 2021; Weiss *et al.*, 2022a). We used the 'diamond-in-water' ablation approach to prepare the samples for solution trace element analyses by ICP-MS (Inductively coupled plasma mass spectrometry) and isotope analyses by TIMS (Thermal ionisation mass spectrometry, Weiss *et al.*, 2022b). As total procedural blanks (TPBs) were too small for the determination of isotope compositions, all isotopic data are presented as measured values. Additional details are given in the Supplementary Information.

High-Density Fluid (HDF) Compositions

Major element compositions of microinclusions in the studied diamonds vary from silicic to low-Mg carbonatitic HDFs and fall within the range of HDF types in fibrous diamonds globally (Fig. 1a). They display a characteristic negative correlation between SiO_2 and CaO, as well as negative covariance between SiO_2 and FeO. There are positive relationships between SiO_2 and Al_2O_3 as well as CaO and P_2O_5. K_2O is relatively uniform (Table S-1), but correlates positively with Cl and negatively with MgO. No systematic spatial (core to rim) compositional change is observed and in most cases microinclusions within a single diamond show variation ≤15 % (1σ) for SiO_2 and K_2O, and ≤20 % for CaO (Table S-1).

The trace element compositions of the HDFs (Table S-2) were published previously by Weiss *et al.* (2022b). Their primitive mantle (PM) normalised patterns are mostly similar and comparable to previously analysed HDFs (Fig. 1b). They exhibit overall decreasing levels from the most incompatible to compatible elements with characteristic anomalies (negative in most cases) of Rb, Nb, Sr, Zr, Hf and Ti, and trace element ratios indicating the involvement of accessory mantle phases in their formations (Weiss *et al.*, 2013). There are no distinctive differences in trace element compositions between the silicic to low-Mg carbonatitic compositions; some trace element ratios show continuous variations irrespective of the major element compositional change (*e.g.*, La/Nb, Zr/Eu; Fig. 1, 2c; Table S-2).

The HDF's Sr and Nd isotope compositions vary between $^{87}Sr/^{86}Sr = 0.70438 \pm 1$ (2SE) to 0.71340 ± 3 and $^{143}Nd/^{144}Nd = 0.5126 \pm 1$ to 0.51177 ± 3 (εNd = −0.2 to −16.9; Fig. 2a; Table S-3). They show a general inverse Sr-Nd isotope correlation from bulk silicate Earth (BSE; Zindler and Hart, 1986) and South African kimberlite (Becker and Le Roex, 2006) values to more radiogenic $^{87}Sr/^{86}Sr$ and unradiogenic $^{143}Nd/^{144}Nd$ ratios, which trend through South African olivine lamproites (formerly Group II kimberlites or orangeite; Becker and Le Roex, 2006) towards the range of continental crust compositions (Rudnick, 1990; Thompson *et al.*, 2007). $^{147}Sm/^{144}Nd$ ratios vary between 0.0669 ± 2 to 0.0970 ± 1 and show a general negative relationship with $^{143}Nd/^{144}Nd$ (Fig. 2b; Table S-3). The analysed diamond samples with a TPB contribution of <10 % for Pb (4 of 7; Table S-3), vary between 17.516 ± 2 and 18.149 ± 3 for $^{206}Pb/^{204}Pb$, 15.53 ± 3 and 15.680 ± 3 for $^{207}Pb/^{204}Pb$ and 37.424 ± 6 and 38.412 ± 8 for $^{208}Pb/^{204}Pb$. These Pb isotope variations are between depleted to enriched mantle components for $^{208}Pb/^{204}Pb$ *vs.* $^{206}Pb/^{204}Pb$, but extend to more radiogenic $^{207}Pb/^{204}Pb$ values above the Pb mantle array (Fig. S-1; Hart *et al.*, 1992; Stracke, 2012). They exhibit a strong positive correlation with Sr isotope compositions (Fig. 3).

The samples define a broad linear negative correlation between $^{143}Nd/^{144}Nd$ and La/Nb (Fig. 2c). Similar inverse relationships are observed between $^{143}Nd/^{144}Nd$ and La/Rb or La/Zr, whereas direct relationships are observed with Sr* ($Sr/\sqrt{(Pr \times Nd)}$) and Zr/Eu ratios (not shown; Tables S-2, S-3). Sr and Pb isotopes plotted against the same trace element ratios exhibit opposite correlations to those with Nd isotopes. These relationships are consistent with the general positive relationship between Sr isotopes and (La, Ba)/(Nb, Zr) ratios in HDFs (Klein-BenDavid *et al.*, 2014). In comparison, no relationship is observed between Sr, Nd, or Pb isotopes and major element compositions; for example, HDF of silicic and low-Mg carbonatitic compositions (diamond 505 and 508) have almost identical Sr and Nd isotope ratios, whereas similar silicic HDFs (diamond 502 and 505) exhibit varying isotopic compositions (Fig. 1, 2, 3; Tables S-1, S-3). These major element-radiogenic isotope systematics are similar to the decoupling between major and trace elements of HDFs from different lithospheric provinces worldwide (Weiss *et al.*, 2022a).

Considering the concentration and unaggregated nature of nitrogen in the studied diamonds, and a likely average mantle residence temperature of ≥950 °C (Stachel and Harris, 2008;

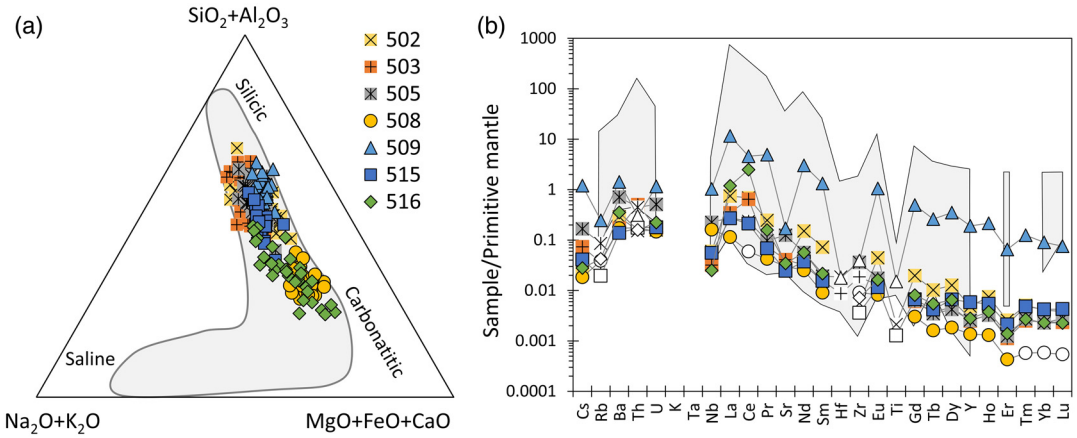

Figure 1 Major and trace element composition of HDF microinclusions in fibrous diamonds. **(a)** $SiO_2 + Al_2O_3$–$Na_2O + K_2O$–MgO + FeO + CaO ternary diagram (in wt. %, on carbon- and water-free basis), showing the compositional range of HDFs in the studied diamonds (see key for sample symbols). Each datapoint represents an individual microinclusion. Data compared to the global variation between silicic, carbonatitic and saline HDF types (shaded area – Weiss and Goldstein, 2018). **(b)** Primitive mantle normalised (McDonough and Sun, 1995) trace element patterns of the HDFs compared to microinclusion-bearing diamonds (shaded area – Klein-BenDavid *et al.*, 2010, 2014). White-filled symbols are data falling between LOQ and LOD (between 10× σ and 3 × σ of the TPBs), and are regarded as qualitative (see details in the Supplementary Information).

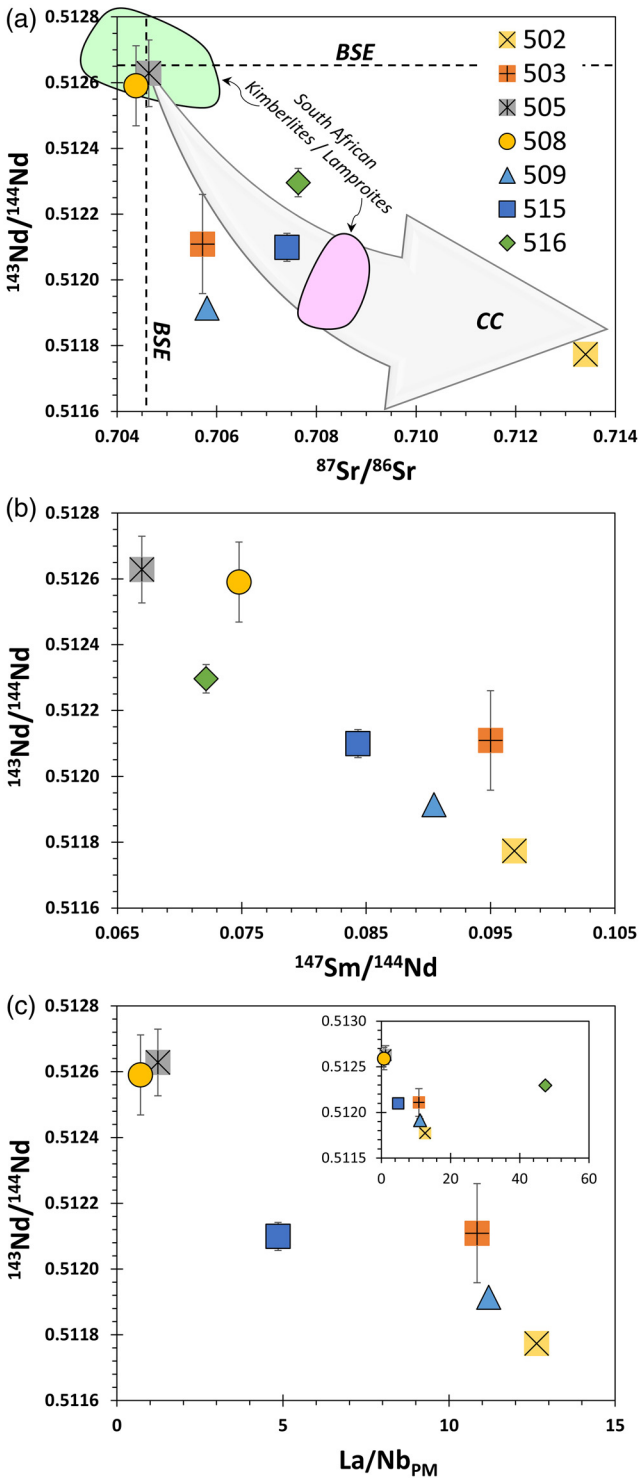

Figure 2 Isotopic and trace element relationships of the HDFs. **(a)** $^{143}Nd/^{144}Nd$ *vs.* $^{87}Sr/^{86}Sr$. Also plotted are the range of South African kimberlite and lamproites (Becker and Le Roex, 2006), bulk silicate Earth (BSE; Zindler and Hart, 1986), and the vector toward continental crust (CC arrow; Rudnick, 1990; Thompson *et al.*, 2007). **(b)** $^{143}Nd/^{144}Nd$ *vs.* $^{147}Sm/^{144}Nd$; the latter is calculated from isotope dilution data (Table S-3). **(c)** $^{143}Nd/^{144}Nd$ *vs.* primitive mantle normalised La/Nb_{PM} ratios; the inset includes diamond 516, which deviates from the general trend. Error bars represent ±2 SE and in most cases are smaller than the symbols.

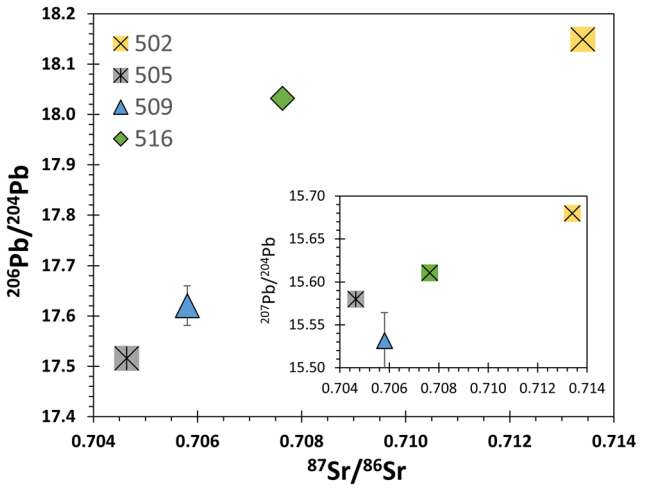

Figure 3 Relationship between Pb and Sr isotope compositions of the HDFs. $^{206}Pb/^{204}Pb$ ratios are shown in the main panel and $^{207}Pb/^{204}Pb$ ratios in the inset. Error bars represent ±2 SE, which in most cases are smaller than the symbols.

Weiss *et al.*, 2022a), their formation could take place from immediately prior to kimberlite eruption up to a maximum of 1 Ga before eruption (Taylor *et al.*, 1996). As the exact timing is unknown, a conservative correction for the isotopic composition of the HDFs is the possible range for the diamond emplacement age between 45–550 Ma, *i.e.* the age range of their possible Canadian host kimberlites (see Supplementary Information). Initial ratios corrected for 45 Ma are almost indistinguishable from measured values. Initial ratios based on 550 Ma are lower by 0.0005 to 0.0010 for $^{87}Sr/^{86}Sr$ compared to the measured values, 0.00024 to 0.00035 for $^{143}Nd/^{144}Nd$, 0.009 to 0.116 for $^{206}Pb/^{204}Pb$, 0.0005 to 0.0068 for $^{207}Pb/^{204}Pb$, and 0.008 to 0.073 for $^{208}Pb/^{204}Pb$ (Fig. 4). The important observation, however, is that the relationships and variations between Sr, Nd and Pb isotopes and between isotopes and trace element compositions persist and all samples have relatively high $^{207}Pb/^{204}Pb$ (Figs. S1 and S2). This remains even if 1 Ga initial ratios are calculated.

HDF Sources

The combined Sr-Nd-Pb isotope signature is not related to radiogenic ingrowth after HDFs were encapsulated in the diamonds during formation, but rather indicates the involvement of two sources with distinct isotopic compositions. This conclusion is established by the inverse correlation on the Sm-Nd isochron diagram (Fig. 2b), the spectrum of Sr and Nd isotopes and the linear relationship between Pb and Sr isotopes that indicate mixing of different endmember components (Fig. 2a and Fig. 3). The covariations of isotopic composition and trace element ratios further support mixing of two components (*e.g.*, Fig. 2c). Klein-BenDavid *et al.* (2010, 2014) also argued for two-component mixing to explain the Sr isotope variations of HDFs, and suggested the involvement of convecting mantle and ancient subcontinental lithospheric mantle (SCLM). Indeed, an SCLM that experienced long-term LREE enrichment (low Sm/Nd) and increased Rb/Sr and U/Pb is required to explain the unradiogenic Nd and radiogenic Sr and Pb isotope endmember compositions of the HDFs studied here. However, the radiogenic $^{207}Pb/^{204}Pb$ values of all of these HDFs, including those with Sr-Nd isotope compositions closest to BSE values, are significantly higher than the compositions of recent ocean island basalts. This is evidence of elevated U/Pb ratios in early Earth history for the source of both endmembers, and precludes major involvement of mantle of asthenospheric origin (Fig. S-1).

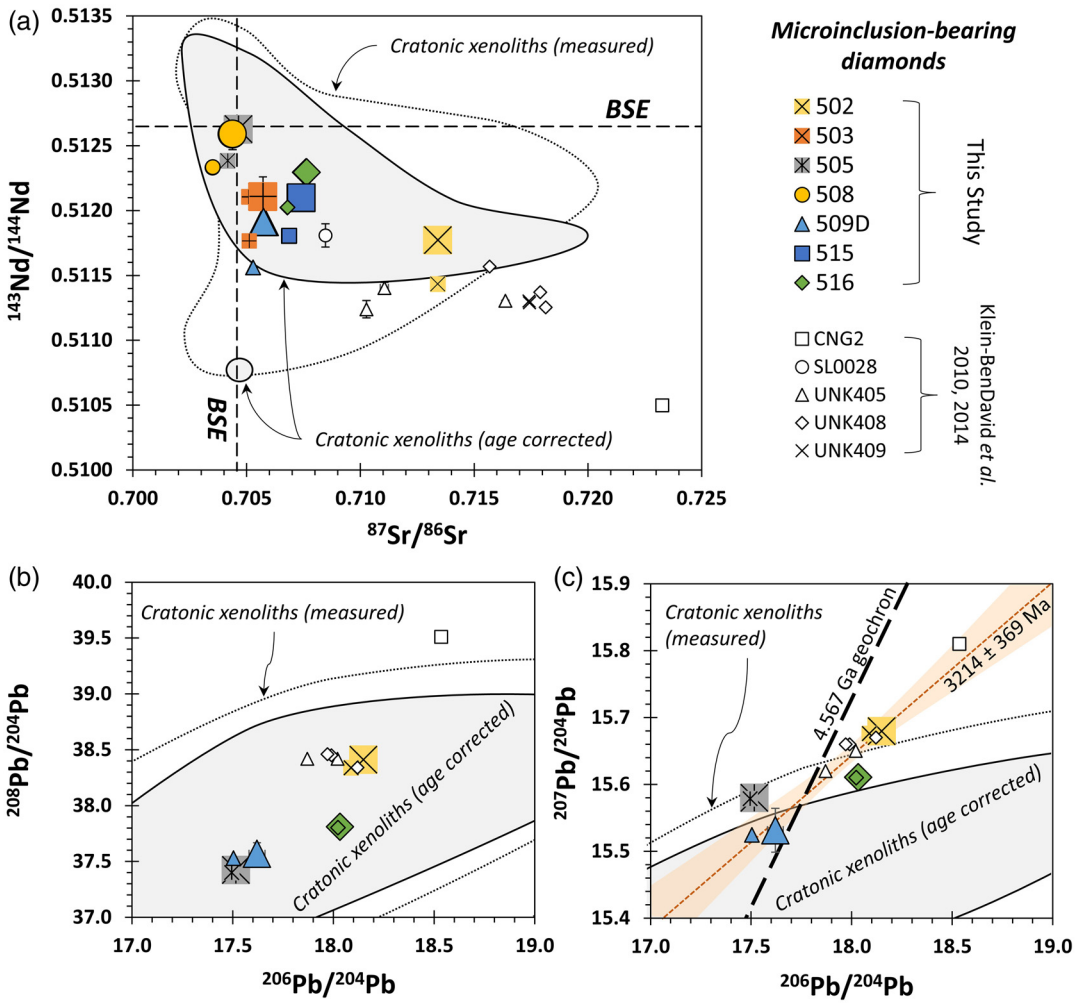

Figure 4 Sr-Nd-Pb isotope compositions of HDF in fibrous diamonds. **(a)** $^{143}Nd/^{144}Nd$ *vs.* $^{87}Sr/^{86}Sr$. Measured values (large coloured symbols) and initial ratios corrected for a maximum possible emplacement age of 550 Ma (small coloured symbols) are presented. Available published data for 5 diamonds from Botswana (UNK; all duplicate analyses are presented), Snap Lake (SL) and Congo (CNG) are also shown (small open symbols; Klein-BenDavid *et al.*, 2010, 2014). The isotopic range of cratonic continental lithosphere determined on whole rock xenolith data (dotted white area - measured values, and lined shaded area – age corrected initial values, based on the PetDB database; http://www.earthchem.org/petdb), and BSE (Zindler and Hart, 1986) are presented for comparison. **(b)** $^{208}Pb/^{204}Pb$ *vs.* $^{206}Pb/^{204}Pb$, and **(c)** $^{207}Pb/^{204}Pb$ *vs.* $^{206}Pb/^{204}Pb$; symbols and areas as in **(a)**. The locus of compositions that developed undisturbed from primitive-mantle lead since Earth's formation is shown for reference (geochron; long dashed black line); the regression line through all the HDF data yields an age of 3214 ± 369 Ma (dashed orange line and 95 % confidence interval).

Figure 4a shows that the Sr and Nd isotope spectrum of the SCLM, as inferred by global whole rock xenolith data from cratons, covers the complete isotopic range of the HDFs studied here. A comparable picture is revealed for $^{208}Pb/^{204}Pb$ and $^{206}Pb/^{204}Pb$ variations, but not for $^{207}Pb/^{204}Pb$, which reach higher values than recorded in SCLM whole-rock initial values (Fig. 4a,b). There is, however, evidence of ancient U enrichment in SCLM-derived xenoliths (Cohen *et al.*, 1984; Davies and Lloyd, 1986) and magmas (*i.e.* Western Australian lamproites; Fraser *et al.*, 1985) that are characterised by highly radiogenic $^{207}Pb/^{204}Pb$ at relatively unradiogenic $^{206}Pb/^{204}Pb$ compositions, some of which overlap the HDFs values.

A strong connection has previously been established between hydrous/carbonated eclogite lithologies (and pyroxenites) with silicic to low-Mg carbonatitic HDF types, comparable in composition to HDFs in the present study (Weiss *et al.*, 2022a). The Sr-Nd-Pb isotope compositions of eclogite and pyroxenite xenoliths (occasionally diamondiferous) are extremely diverse, from highly unradiogenic to highly radiogenic values (*e.g.*, Jacob, 2004; Xu *et al.*, 2009; Aulbach *et al.*, 2019). Although there is limited available data from such xenoliths, their isotope variation overlaps most of the SCLM spectrum and HDFs (Fig. S-2). In addition, a large isotopic range was documented for eclogites from individual locations (Jacob, 2004; Aulbach *et al.*, 2019). Such sources for the HDF studied here can explain their silicic to low-Mg carbonatitic major element compositions and their varying radiogenic isotope signatures (Fig. 1a and Fig. 4; Table S-1 and S-3).

Previously published Sr-Nd (±Pb) isotope data are limited to 5 additional microinclusion-bearing diamonds from Canada, Botswana and Congo, all with silicic to low-Mg carbonatitic HDF compositions (Klein-BenDavid *et al.*, 2010, 2014; Timmerman *et al.*, 2019). Figure 4 shows that these HDFs overlap and expand the isotopic trends of the studied HDFs towards more unradiogenic Nd and radiogenic Sr and Pb compositions. These Sr-Nd isotope ratios overlap sediments derived from old continental crust (Goldstein and Jacobsen, 1987), suggesting their possible contribution to the formation of HDFs through subduction. Such a connection is consistent with the correlation between La/Nb and isotopes (Fig. 2c and Fig. 6e in Klein-BenDavid *et al.*,

2014), implying the involvement of a recycled component, and may also explain the radiogenic $^{207}Pb/^{204}Pb$ signature of all of these HDFs (Fig. 4c, Fig. S-1 and Fig. 8 of Klein-BenDavid *et al.*, 2014). Remarkably, the $^{207}Pb/^{204}Pb$ *vs.* $^{206}Pb/^{204}Pb$ composition of the HDFs define a positive trend (Fig. 4c). Klein-BenDavid *et al.* (2014) suggested that the Pb isotope signature of the most radiogenic HDF indicates a multi-stage evolution of its source, characterised by an Archean enrichment event, which increased the U/Pb ratios (μ), followed by a more recent event that led to lower μ. Although there is no unique solution to explain the data, such a scenario fits all of the HDF data. Thus, the $^{207}Pb/^{204}Pb$ *vs.* $^{206}Pb/^{204}Pb$ trend may be interpreted as an age that corresponds to 3214 ± 369 Ma (Fig. 4c). However, this trend is more likely the manifestation of mixing of two isotopic endmember source components that differ in age significantly. Calculated Nd T_{DM} model ages for the HDFs sources suggest an age range between 0.5 and 1.8 Ga (although these ages are minimum estimates because HDF formation produces LREE enrichment which reduces the model ages; Goldstein *et al.*, 1984). The most unradiogenic HDF sample reported by Klein-BenDavid *et al.* (2014) yields a T_{DM} of 2.6 Ga.

In summary, the relationships between isotope and trace element ratios of silicic to low Mg-carbonatitic HDFs indicate the involvement of two distinct eclogite/pyroxenite-dominated sources within the continental lithosphere: one with a relatively primitive Sr-Nd isotope composition and another with unradiogenic Nd and radiogenic Sr and Pb isotope ratios. We propose that the latter source reflects an old metasomatic event in the Canadian continental root by fluid addition from a subducting slab (most probably involving the Slave Craton in the Paleoproterozoic, ≥1.8 Ga, *e.g.,* Wopmay collisional event). Near-solidus melting of this source during a subsequent tectono-magmatic event led to the formation of HDFs with unradiogenic Nd and radiogenic Sr and Pb isotope ratios. Simultaneous melting of a more primitive source introduced HDFs with less enriched Sr-Nd isotope signature, and mixing of the two HDF endmember components formed silicic to low-Mg carbonatitic HDFs with the observed range of Sr-Nd-Pb isotope compositions (Fig. 4). Formation of either HDF endmember in one of the sources, which percolates through and interacts with the other source, would lead to equivalent results. Either way, the HDFs' host diamonds crystallised during this event. The relatively short mantle residence time of these diamonds, indicated by their unaggregated nitrogen, suggests that the Sr-Nd-Pb isotopic signature of the subducting component, most notably the relatively elevated $^{207}Pb/^{204}Pb$ was formed in, or was added to, the cratonic continental lithosphere long before HDF formation and inclusion in diamonds. Comparable isotope-trace element relationships in silicic- to low-Mg carbonatitic-bearing diamonds from different continents suggest that the same processes, including sediment subduction, impacted other SCLM provinces producing the source of diamond-forming fluids.

Acknowledgements

We thank S. Jockusch for help with the ablations of diamond-in-water, O. Elazar for help with column chemistry and Sr isotope analyses, and M. Schrauder for the donation of diamonds used in this study. We thank Graham Pearson, Emma Tomlinson and an anonymous reviewer, as well as GPL Editor Ambre Luguet for detailed and constructive reviews. Y.W. acknowledges support by ISF Grants No. 2015/18 and 779/22, NSF Grant EAR-1348045 and Europlanet 2020 RI Grant 18-EPN5-002. Europlanet 2020 RI has received funding from the European Union's Horizon 2020 research and innovation programme under grant agreement No. 654208.

Editor: Ambre Luguet

Additional Information

Supplementary Information accompanies this letter at https://www.geochemicalperspectivesletters.org/article2329.

Cite this letter as: Weiss, Y., Koornneef, J.M., Davies, G.R. (2023) Sr-Nd-Pb isotopes of fluids in diamond record two-stage modification of the continental lithosphere. *Geochem. Persp. Let.* 27, 20–25. https://doi.org/10.7185/geochemlet.2329

References

Akagi, T., Masuda, A. (1988) Isotopic and elemental evidence for a relationship between kimberlite and Zaire cubic diamonds. *Nature* 336, 665–667. https://doi.org/10.1038/336665a0

Aulbach, S., Heaman, L.M., Jacob, D.E., Viljoen, K.S. (2019) Ages and sources of mantle eclogites: ID-TIMS and in situ MC-ICPMS Pb-Sr isotope systematics of clinopyroxene. *Chemical Geology* 503, 15–28. https://doi.org/10.1016/j.chemgeo.2018.10.007

Becker, M., Le Roex, A.P. (2006) Geochemistry of South African on- and off-craton, Group I and Group II kimberlites: Petrogenesis and source region evolution. *Journal of Petrology* 47, 673–703. https://doi.org/10.1093/petrology/egi089

Cohen, R.S., O'Nions, R.K., Dawson, J.B. (1984) Isotope geochemistry of xenoliths from East Africa: Implications for development of mantle reservoirs and their interaction. *Earth and Planetary Science Letters* 68, 209–220. https://doi.org/10.1016/0012-821X(84)90153-5

Davies, G., Lloyd, F. (1986) Sub-continental lithosphere beneath Katew-Kikorongo, SW Uganda. *International Kimberlite Conference: Extended Abstracts* 4, no. 1, 229–231. https://doi.org/10.29173/ikc1126

Dawson, J.B. (1984) Contrasting Types of Upper-Mantle Metasomatism? In: Kornprobst, J. (Ed.), *Developments in Petrology*, 11, 289–294. https://doi.org/10.1016/B978-0-444-42274-3.50030-5

Fraser, K.J., Hawkesworth, C.J., Erlank, A.J., Mitchell, R.H., Scott-Smith, B.H. (1985) Sr, Nd and Pb isotope and minor element geochemistry of lamproites and kimberlites. *Earth and Planetary Science Letters* 76, 57–70. https://doi.org/10.1016/0012-821X(85)90148-7

Goldstein, S.J., Jacobsen, S.B. (1987) The Nd and Sr isotopic systematics of river-water dissolved material: Implications for the sources of Nd and Sr in seawater. *Chemical Geology: Isotope Geoscience Section* 66, 245–272. https://doi.org/10.1016/0168-9622(87)90045-5

Goldstein, S.L., O'Nions, R.K., Hamilton, P.J. (1984) A Sm-Nd isotopic study of atmospheric dusts and particulates from major river systems. *Earth and Planetary Science Letters* 70, 221–236. https://doi.org/10.1016/0012-821X(84)90007-4

Hart, S.R., Hauri, E.H., Oschmann, L.A., Whitehead, J.A. (1992) Mantle plumes and entrainment – isotopic evidence. *Science* 256, 517–520. https://doi.org/10.1126/science.256.5056.517

Jacob, D. (2004) Nature and origin of eclogite xenoliths from kimberlites. *Lithos* 77, 295–316. https://doi.org/10.1016/j.lithos.2004.03.038

Kempe, Y., Weiss, Y., Chinn, I., Navon, O. (2021) Multiple metasomatic diamond-forming events in a cooling lithosphere beneath Voorspoed, South Africa. *Lithos*, 106285. https://doi.org/10.1016/j.lithos.2021.106285

Klein-BenDavid, O., Pearson, D.G., Nowell, G.M., Ottley, C., McNeill, J.C.R., Cartigny, P. (2010) Mixed fluid sources involved in diamond growth

constrained by Sr–Nd–Pb–C–N isotopes and trace elements. *Earth and Planetary Science Letters* 289, 123–133. https://doi.org/10.1016/j.epsl.2009.10.035

Klein-BenDavid, O., Pearson, D.G., Nowell, G.M., Ottley, C., McNeill, J.C.R., Logvinova, A., Sobolev, N.V. (2014) The sources and time-integrated evolution of diamond-forming fluids – Trace elements and isotopic evidence. *Geochimica et Cosmochimica Acta* 125, 146–169. https://doi.org/10.1016/j.gca.2013.09.022

McDonough, W.F., Sun, S.S. (1995) The composition of the Earth. *Chemical Geology* 120, 223–253. https://doi.org/10.1016/0009-2541(94)00140-4

Rudnick, R.L. (1990) Nd and Sr isotopic compositions of lower-crustal xenoliths from north Queensland, Australia: Implications for Nd model ages and crustal growth processes. *Chemical Geology* 83, 195–208. https://doi.org/10.1016/0009-2541(90)90280-K

Smith, E.M., Kopylova, M.G., Nowell, G.M., Pearson, D.G., Ryder, J. (2012) Archean mantle fluids preserved in fibrous diamonds from Wawa, Superior craton. *Geology* 40, 1071–1074. https://doi.org/10.1130/G33231.1

Stachel, T., Harris, J.W. (2008) The origin of cratonic diamonds — Constraints from mineral inclusions. *Ore Geology Reviews* 34, 5–32. https://doi.org/10.1016/j.oregeorev.2007.05.002

Stracke, A. (2012) Earth's heterogeneous mantle: A product of convection-driven interaction between crust and mantle. *Chemical Geology* 330, 274–299. https://doi.org/10.1016/j.chemgeo.2012.08.007

Taylor, W.R., Canil, D., Milledge, H.J. (1996) Kinetics of Ib to IaA nitrogen aggregation in diamond. *Geochimica et Cosmochimica Acta* 60, 4725–4733. https://doi.org/10.1016/S0016-7037(96)00302-X

Thompson, R.N., Riches, A.J.V., Antoshechkina, P.M., Pearson, D.G., Nowell, G.M., Ottley, C.J., Dickin, A.P., Hards, V.L., Nguno, A.-K., Niku-Paavola, V. (2007) Origin of CFB Magmatism: Multi-tiered Intracrustal Picrite–Rhyolite Magmatic Plumbing at Spitzkoppe, Western Namibia, during Early Cretaceous Etendeka Magmatism. *Journal of Petrology* 48, 1119–1154. https://doi.org/10.1093/petrology/egm012

Timmerman, S., Yeow, H., Honda, M., Howell, D., Jaques, A.L., Krebs, M.Y., Woodland, S., Pearson, D.G., Ávila, J.N., Ireland, T.R. (2019) U-Th/He systematics of fluid-rich 'fibrous' diamonds – Evidence for pre- and syn-kimberlite eruption ages. *Chemical Geology* 515, 22–36. https://doi.org/10.1016/j.chemgeo.2019.04.001

Turner, S., Turner, M., Bourdon, B., Cooper, K., Porcelli, D. (2021) Extremely young melt infiltration of the sub-continental lithospheric mantle. *Physics of the Earth and Planetary Interiors* 313, 106325. https://doi.org/10.1016/j.pepi.2019.106325

Weiss, Y., Griffin, W.L., Navon, O. (2013) Diamond-forming fluids in fibrous diamonds: The trace-element perspective. *Earth and Planetary Science Letters* 376, 110–125. https://doi.org/10.1016/j.epsl.2013.06.021

Weiss, Y., McNeill, J., Pearson, D.G., Nowell, G.M., Ottley, C.J. (2015) Highly saline fluids from a subducting slab as the source for fluid-rich diamonds. *Nature* 524, 339–342. https://doi.org/10.1038/nature14857

Weiss, Y., Goldstein, S.L. (2018) The involvement of diamond-forming fluids in the metasomatic 'cocktail' of kimberlite sources. *Mineralogy and Petrology*, 1–19. https://doi.org/10.1007/s00710-018-0613-8

Weiss, Y., Czas, J., Navon, O. (2022a) Fluid inclusions in fibrous diamonds. *Reviews in Mineralogy and Geochemistry* 88, 475–532. https://doi.org/10.2138/rmg.2022.88.09

Weiss, Y., Jockusch, S., Koornneef, J.M., Elazar, O., Davies, G.R. (2022b) Laser ablation of 'diamonds-in-water' for trace element and isotopic composition analysis. *Journal of Analytical Atomic Spectrometry* 37, 1431–1441. https://doi.org/10.1039/D2JA00088A

Xu, W.-L., Gao, S., Yang, D.-B., Pei, F.-P., Wang, Q.-H. (2009) Geochemistry of eclogite xenoliths in Mesozoic adakitic rocks from Xuzhou-Suzhou area in central China and their tectonic implications. *Lithos* 107, 269–280. https://doi.org/10.1016/j.lithos.2008.11.004

Zindler, A., Hart, S. (1986) Chemical Geodynamics. *Annual Review of Earth and Planetary Sciences* 14, 493–571. https://doi.org/10.1146/annurev.ea.14.050186.002425

Geochemical Perspectives Letters

Sr-Nd-Pb isotopes of fluids in diamond record two-stage modification of the continental lithosphere

Y. Weiss, J.M. Koornneef, G.R. Davies

Supplementary Information

The Supplementary Information includes:

- Sample Description
- Fourier-transform infrared (FTIR) spectroscopy
- Microinclusion major elements analyses
- Diamond ablation and processing
- Trace elements and radiogenic isotopes analyses
- Tables S-1 to S-3
- Figures S-1 to S-2
- Supplementary Information References

Sample Description

Seven microinclusion-bearing fibrous diamonds from a single source in Canada were selected for the present study from a private collection of M. Schrauder (Vienna, Austria). The exact origin of these diamonds is unknown; however, based on the year of first mine production compared to when these diamonds were originally acquired (2009), potential mines are Diavik (with an emplacement age of 55–56 Ma; Graham *et al.*, 1999; Creaser *et al.*, 2004), Ekati (45–75 Ma; Lockhart *et al.*, 2003; Creaser *et al.*, 2004), Jericho (~172 Ma; Heaman *et al.*, 2002), Victor (170–180 Ma; Januszczak *et al.*, 2013) or Snap Lake (523–535 Ma; Agashev *et al.*, 2001; Heaman *et al.*, 2004). The diamonds are all 3 to 4 mm in diameter, vary in weight between 91 to 116 mg, have cubic morphology, and are white to dark grey in colour. Five of the diamonds are fully fibrous whereas two (515 and 516) have a fibrous coat overgrowth on a small microinclusion-free octahedral core (<800 µm across). Each diamond was laser-cut twice to create two parallel side sections and a central thin plate that was polished on both sides; all parts were then cleaned ultrasonically in a mixture of concentrated HF (29 N) and HNO_3 (16 N) for >2 h and washed with ethanol and distilled water.

Fourier-transform infrared (FTIR) spectroscopy

Infrared spectra were collected using a Thermo Scientific Nicolet RaptIR microscope coupled to an iS50 spectrometer (Polaris mid-IR source, KBr beamsplitter, MCT-A detector, He–Ne laser) at the Hebrew University of Jerusalem. Spectra were taken in the range of 650–4000 cm^{-1} with a resolution of 2 cm^{-1}. Nitrogen concentrations and aggregation were determined with a modified version of the DiaMap freeware (Howell *et al.*, 2012, 2017).

Microinclusion Major Elements Analyses

The major element composition of high-density fluid (HDF) microinclusions was determined on inclusions immediately beneath the polished surface (<2 μm depth) using a JEOL JXA-8230 EPMA at the Hebrew University of Jerusalem. Each inclusion was analysed for 100 s by energy dispersive spectrometry, using a focused electron beam (1 μm) at 15 kV and 15 nA (Kempe *et al.*, 2021; Weiss *et al.*, 2022a). The spectral data were reduced using the PRZ correction procedure supplied by JEOL. Concentrations of Si, Ti, Al, Cr, Fe, Mg, Ca, Na, K, P, and Cl were determined from the integrated number of counts of their Kα peaks. Ba, S, and F were measured using wavelength dispersive spectrometry and combined with the other elements. Oxygen was calculated by stoichiometry. The total amount of oxides + chlorine in each analysis varied between 1 and 9 wt. %, with an average of 3.2 ± 1.4 wt. % for all 236 analysed microinclusions. The low and variable sums reflect the small size of the inclusions, variable depth beneath the surface, and their high content of undetected water and carbonate. Precision is approximately 2 σ (%) = 2/oxide in wt. % (Jablon and Navon, 2016), and is <50 % for oxide concentrations of 0.05 wt. %, <15 % for 0.25 wt. %, <10 % for 0.5 wt. % and <5 % for 1 wt. %. The major oxides + Cl concentrations were normalised to 100 % on a carbon-free and volatiles-free basis, and the average composition of the HDF in each diamond was calculated (Table S-1).

Diamond Ablation and Processing

We used the 'diamond-in-water' ablation approach of Weiss *et al*. (2022b) to prepare the samples for solution trace elements and isotopic analyses. All preparation, post-ablation processing, and digestion took place in a PicoTrace Ultra-Clean laboratory at Lamont-Doherty Earth Observatory (LDEO) while laser ablation was carried out in the Department of Chemistry of Columbia University. Each diamond was weighed 3 times using a Mettler Toledo XP6 microbalance, before and after ablation, to determine the weight of the ablated material with a precision of ±1 μg. Ablation took place in a custom-modified quartz Fluorometer cell (3-Q-20, 7.0 ml, Starna Cells) as an ablation cell. The Fluorometer cell was cleaned in 8 N double-distilled (DD) HNO_3 for a minimum of 7 days and PTFE parts were cleaned in 16 N DD HNO_3 at 180 °C for 4 hours before they were stored in 8 N DD HNO_3; all parts were rinsed in milli-Q water before use. Each diamond was cleaned in a mixture of 16 N DD HNO_3 and 29 N DD HF on a hotplate at 120 °C for several hours, then rinsed in milli-Q water and mounted by a tailored PTFE ring into the PTFE holder (+ lid), before it was placed in the cell and milli-Q water was added. The cell was then sealed. Diamond-in-water ablation was performed using a Spectra-Physics GCR-150-30 Q-switched Nd:YAG laser (532 nm, 150 mJ/pulse, 7 ns pulse duration, 30 Hz repetition rate). Following ablation, the cell was opened and the solution containing the ablated material was transferred to a clean PFA beaker. An additional 1 ml of milli-Q water was used to wash the ablation cell and transferred to the beaker, before drying down at 80 °C. The sample was then digested using a 1.2 ml mixture (5:1) of 16 N DD HNO_3 and 29 N DD HF at 120 °C, dried down again at 80 °C and re-dissolved in 1 ml of 1 N DD HNO_3 before analyses. An aliquot of 200 μl of each sample solution was separated for trace elements analyses and the remaining 800 μl was processed for Sr-Nd-Sm-Pb isotope measurements.

Trace Elements and Radiogenic Isotopes Analyses

Trace element concentrations were determined using a VG PlasmaQuad ExCell quadrupole ICPMS at LDEO. The 200 μl aliquot of each sample solution was diluted to 1 ml using 3 % DD HNO_3, and introduced to the ICPMS with a desolvation system (CETAC Aridus), which enhances sensitivity and reduces solvent-based interferences (i.e., oxides and hydrides). Solution concentrations were determined against 6 point calibration lines of an in-house multi-element standard, spanning the expected concentration range, and an internal standard of 1 ppb In. All concentrations were corrected for instrumental drift and for the average total procedural blank values, and

normalised to the weight of the ablated material of each diamond (Table S-2). Errors are estimated at ~2 %, based on the laboratory multiple runs of a calibration curve from repeated measurements of in-house multi-element solutions and rock standards.

Chemical separation of Sr, Nd, Sm and Pb from the 800 µl aliquot of each sample solution were performed at Vrije Universiteit Amsterdam (VU) using a miniaturised chromatographic separation procedures, followed by isotopic analysis by TIMS using a Thermo Scientific TRITON Plus instrument equipped with 10^{11} and 10^{13} Ω resistors (Koornneef *et al.*, 2014, 2015; Klaver *et al.*, 2016; Weiss *et al.*, 2022b). Pb was separated first and divided by weight to 'natural' and 'spiked' fractions (~66.6 % and 33.3 %, respectively), the latter was spiked using an in-house VU_^{207}Pb-^{204}Pb mix standard with a ratio of 0.79086±7 calibrated against standard reference material NIST SRM 982 (Thirlwall, 2002). Both fractions were dried down, nitrated twice with 2 drops of concentrated HNO_3 to eliminate organic material, and re-dissolved in 2 µl 10 % HNO_3 before they were loaded together with 1.5 µl silica gel activator on pre-cleaned outgassed zone-refined rhenium filaments. The natural sample fractions were analysed using a 10^{13} Ω resistor for the detection of ^{204}Pb in combination with regular 10^{11} Ω resistors for the other isotopes (the online tau correction was used to account for different response times); all were run to exhaustion. Spiked fractions were analysed using 10^{11} Ω resistors. As the double spike inversion cannot be solved algebraically, each sample was processed in an offline spreadsheet. Both natural and spiked data were subjected to an artificial mass fractionation correction that allows a realistic estimate of the analytical uncertainties. The corrected data were subjected to a 2 σ outlier test, algebraic error propagation, and instrumental mass fractionation correction. Uncertainties were propagated algebraically and take into account the strong error correlation (r >0.90) between ^{20x}Pb/^{204}Pb ratios. Instrumental reproducibility during analyses was monitored using an NBS981 standard of 40 and 2 ng Pb. An aliquot solution of BHVO-2 containing ~130 pg was processed along with the individual sample batches to monitor and ensure data quality; it gave ^{206}Pb/^{204}Pb = 18.55 ± 21, ^{207}Pb/^{204}Pb = 15.502 ± 20 and ^{208}Pb/^{204}Pb = 38.089 ± 58. The small variation from the Georem values (18.647 ± 24, 15.533 ± 9 and 38.237 ± 18 (Weis *et al.*, 2006)) could result from the small amount that was processed in the present study and a blank contribution or be assigned to the BHVO-2 powder not being homogeneous for Pb as it was processed using a tungsten carbide crushing method. Before Pb column separation, sample solutions were spiked with ^{84}Sr and a ^{149}Sm-^{150}Nd mixed spike aiming for a sample/spike ratio of 20–100 for Sr and 20 for Nd. Sr and REEs were simultaneously separated by placing the Sr column above the TRU column, after which the two-column sets were separated and eluted. Subsequently, the REE fraction was dried down, redissolved, and loaded onto Ln-columns by which Nd and then Sm were separated and collected. The Sr, Nd and Sm fractions were dried down and re-dissolved in 3 µl 10 % HNO_3 before they were loaded together with 1.5 µl activator ($TaCl_5$ 100 ppm for Sr, and 10 % H_3PO_4 for Nd and Sm) on pre-cleaned outgassed rhenium filaments. All Sr samples and two samples with >5 ng Nd (preliminary indicated by ICP-MS analyses) were measured on Faraday cups with 10^{11} Ω resistors, whereas the remaining Nd samples and Sm samples were analysed using 10^{13} Ω resistors. Most samples were run to exhaustion. The Sr, Nd and Sm isotope data are normalised for mass fractionation in the mass spectrometer to overcome any mass fractionation induced by chromatography or mass spectrometry. Instrumental reproducibility during analyses was monitored using an NBS987 standard of 200, 10, 5, and 1 ng Sr, JNDi-1 standard of 200 ng Nd and an in-house CIGO standard of 2 ng and 200 pg Nd, and an Sm standard of 20 ng. BHVO-2 aliquots containing ~35.5 and 3.6 ng Sr and ~2.2 ng and 220 pg Nd, respectively, gave an average ^{87}Sr/^{86}Sr = 0.703538 ± 39 and ^{143}Nd/^{144}Nd = 0.513073 ± 141; in agreement with its reference values 0.703479 ± 20 and 0.512984 ± 11.

For the complete clean lab protocols and procedures, and instrumental measuring routines and cup configuration, the reader is referred to Koornneef *et al*. (2014, 2015), Klaver *et al*. (2016) and Weiss *et al*. (2022b). The measured Sr-Nd-Pb isotope compositions of the analysed diamonds are in Table S-3. Initial values are calculated using the measured isotope ratio by TIMS (TIMS), measured element concentration by isotope dilution (TIMS-ID), and measured element concentration by ICPMS (ICPMS), as follows:

$^{87}Sr/^{86}Sr_{(Initial)} = {}^{87}Sr/^{86}Sr_{(TIMS)} - {}^{87}Rb/^{86}Sr_{(Calculated)} \times (e^{\lambda t} - 1)$, where $^{87}Rb/^{86}Sr_{(Calculated)} = [Rb_{(ICPMS)}/Sr_{(TIMS\text{-}ID)}] \times [2.69295 + 0.2830486 \times {}^{87}Sr/^{86}Sr_{(TIMS)}]$

$^{143}Nd/^{144}Nd_{(Initial)} = {}^{143}Nd/^{144}Nd_{(TIMS)} - {}^{147}Sm/^{144}Nd_{(Calculated)} \times (e^{\lambda t} - 1)$, where $^{147}Sm/^{144}Nd_{(Calculated)} = [Sm_{(TIMS\text{-}ID/ICPMS)}/Nd_{(TIMS\text{-}ID)}] \times [0.531628 + 0.142556 \times {}^{143}Nd/^{144}Nd_{(TIMS)}]$

$^{206}Pb/^{204}Pb_{(Initial)} = {}^{206}Pb/^{204}Pb_{(TIMS)} - {}^{238}U/^{204}Pb_{(Calculated)} \times (e^{\lambda t} - 1)$, where $^{238}U/^{204}Pb_{(Calculated)} = [U_{(ICPMS)} \times 0.9928/238.0289] / [Pb_{(TIMS)} / (1/(1 - {}^{206}Pb/^{204}Pb_{(TIMS)} + {}^{207}Pb/^{204}Pb_{(TIMS)} + {}^{208}Pb/^{204}Pb_{(TIMS)})) / Pb_{(MW,\ g/mole)}]$; similar calculation for $^{207}Pb/^{204}Pb_{(Initial)}$ is made using the natural aboundance of $^{235}U = {}^{238}U/137.88$ and for $^{208}Pb/^{204}Pb_{(Initial)}$ using the $^{232}Th/^{204}Pb_{(Calculated)}$ and $Th_{(ICPMS)}$.

Total procedural blanks

Our total procedural blank (TPB) was treated as samples and incorporates all aspects of the diamond-in-water ablation method (except for ablation itself), including cleaning and preparation of ablation cells and samples, associated ablation practices, post-ablation protocols and chemicals, and instrumental procedures. For trace elements, we consider any measurement above the limit of quantification as quantitative ($LOQ = 10 \times \sigma_{(TPB)}$; where σ is the uncertainty on the blank/background), whereas values between LOQ and the limit of detection are regarded as qualitative ($LOD = 3 \times \sigma_{(TPB)}$; (Currie, 1968). The uncertainty for the two TPBs collected is calculated as $\sigma = |x_{(TPB1)} - x_{(TPB2)}|/\sqrt{2}$ and the LOQ in ppb for each element measured by ICPMS is in Table S-2. These are equivalent to 2–7 × 10^{-4} ng in 1 ml of TPB solution for Cs, Eu, Tb, Ho, Er, Tm and Lu, 1.5–5.5 × 10^{-3} ng for U, Pr, Sm, Gd, Dy and Yb, 1.3–4.3 × 10^{-2} ng for Nd, Hf and Y, 0.1–0.4 ng for Rb, Th, Nb, La and Sr, and in the range of 1.3–2.8 ng for Ba, Ce, Zr and 60 ng for Ti. To evaluate the contribution of the TPB on the isotopic composition of the measured samples, we determined its Sr, Nd, Sm and Pb contents by isotope dilution TIMS analyses (Table S-3). The two TPBs yielded 373 and 382 pg of Sr that make up between 3–8 % by weight of the samples; Nd of 4.8 and 7.9 pg that make up between 0.04–2.1 %; Sm of 0.64 and 1.3 pg that make up 0.04–2.6 %; and Pb of 225 and 239 pg that constitute between 0.887–52 % by weight of the samples. TPBs were too small for the determination of isotope compositions, hence all isotopic data are presented as measured values in Table S-3.

Supplementary Tables

Table S-1 Average major element composition of HDF microinclusions in the analysed diamonds. [a] Oxide average in wt. % after normalisation (avg; on water-free and carbonate-free basis), and its standard deviation (1 sd). [b] Not measured. [c] Initial average analytical totals of oxides and Cl (wt. %) before normalisation.

Diamond	502		503		505		508		509		515		516	
No. of inclusions analysed	25		30		35		28		30		39		49	
Composition (wt. %)	avg	1 sd	avg	1 sd	avg	1 sd	avg	1 sd	avg	1 sd	avg	1 sd	avg	1 sd
SiO_2 [a]	39.5	4.6	44.6	6.8	42.0	4.3	23.8	3.0	47.6	3.3	35.6	3.3	25.7	5.9
TiO_2	2.6	0.9	2.4	1.2	2.5	1.0	2.8	1.6	2.7	1.4	2.7	1.1	2.3	1.1
Al_2O_3	5.3	0.7	5.4	0.9	5.8	1.0	4.1	0.9	4.7	0.8	4.8	1.2	5.1	1.2
Cr_2O_3	--- [b]		0.7	0.3	0.7	0.6	0.7	0.7	1.2	1.0	1.5	1.1	0.8	0.7
FeO	9.3	2.2	9.2	1.7	7.3	1.3	13.4	2.1	9.6	1.6	10.3	1.6	9.4	2.3
MgO	6.4	1.9	4.4	1.3	5.6	0.9	6.5	1.2	6.1	0.8	5.2	1.2	4.7	1.3
CaO	9.1	2.1	6.2	2.5	9.3	1.8	22.1	3.7	7.5	1.6	11.6	2.3	22.2	4.9
BaO	2.6	1.0	0.6	0.5	1.1	0.9	1.2	0.9	0.9	0.8	1.4	0.9	1.3	1.3
Na_2O	4.3	1.3	4.1	1.0	3.9	1.0	5.4	1.4	5.8	1.1	4.7	1.2	4.8	1.0
K_2O	12.7	2.4	15.3	1.4	13.9	1.1	12.0	1.4	9.5	0.9	14.4	1.1	14.7	2.8
P_2O_5	5.7	1.5	5.4	2.2	5.9	1.3	6.7	1.9	4.1	1.2	6.5	2.0	6.4	2.0
Cl	3.1	0.9	2.7	0.8	2.8	0.7	2.7	0.7	1.4	0.7	3.1	0.8	4.5	1.4
SO_3	0.9	0.6	0.6	0.4	0.4	0.3	0.5	0.4	0.5	0.4	0.9	0.7	0.6	0.4
Total [c]	4.5	1.5	3.4	1.5	3.5	1.4	2.4	0.9	3.2	1.2	2.4	0.9	3.2	1.3

Table S-2 Trace element compositions and selected ratios of the HDFs in the analysed diamonds. [a] Concentrations (in ppb) are normalised to the weight of the ablated material. [b] Limit of quantification (LOQ) in ppb is calculated as 10 times the uncertainty on the blank/background, i.e. LOQ = 10 × $\sigma_{(TPB;\ total\ procedural\ blank)}$. [c] Values in red italics are between the LOQ and the limit of detection (LOD), where LOD = 3 × $\sigma_{(TPB)}$. Empty cell - value below LOD. Data for diamonds 502, 505, 508, 509, 515 and 516 are from Weiss *et al.* (2022b); '509C' is the preferred duplicate of 509 for the present study as it has the smallest contribution of TPB on the isotopic composition of the measured samples (see Table 2 of Weiss *et al*., 2022b). [d] Trace element ratios are calculated before rounding off the measured element concentrations.

Diamond	502	503	505	508	509	515	516	LOQ
Ablated material (mg)	11.2	6.5	4.9	9.5	2.8	14.4	9.7	
Element (ppb) [a]								
Cs	0.48	1.5	3.5	0.39	25.2	0.86	0.59	0.0004 [b]
Rb		*21.5* [c]	*51.4*	*23.3*	148	*11.7*	*25.4*	0.41
Ba	1912	1133	4698	1131	9404	916	2333	2.6
Th	*12.1*	39.9	*35.5*	*13.9*	*23.8*	*13.9*	*12.6*	0.21
U	3.2	3.5	10.3	3.0	23.5	3.6	4.5	0.0055
Nb	39.1	21.1	148	106	683	36.7	16.6	0.11
La	486	225	180	74.5	7532	175	774	0.36
Ce	1150	1081	*394*	*99.1*	7735	355	4168	2.8
Pr	62.4	18.8	24.8	10.8	1254	17.4	40.2	0.0051
Sr	643	815	2486	605	3393	489	686	0.26
Nd	189	40.3	70.6	31.4	3787	46.9	70.6	0.013
Sm	29.4	6.3	7.9	3.7	538	6.3	8.8	0.0048
Hf		*2.5*	*5.3*		*5.0*			0.044
Zr	*58.7*	*195*	382	*95.6*	*411*	*37.8*	*75.5*	1.3
Eu	6.8	2.0	2.7	1.3	163	1.8	2.5	0.0006
Ti	*2548*				*18137*	*1539*		60.7
Gd	10.7	3.3	3.5	1.6	271	3.6	4.4	0.0015
Tb	1.0	0.37	0.34	0.16	25.8	0.41	0.54	0.0002
Dy	8.6	3.2	2.8	1.2	236	4.5	4.4	0.0030
Y	21.0	10.7	11.1	5.8	821	25.2	12.0	0.013
Ho	1.1	0.50	0.48	0.19	32.1	0.81	0.56	0.0004
Er	1.1	0.49	0.54	0.19	28.5	0.93	0.61	0.0007
Tm	0.34	0.17	0.18	*0.04*	8.5	0.33	0.18	0.0006
Yb	1.8	1.1	1.0	*0.26*	39.7	1.9	1.0	0.0040
Lu	0.26	0.16	0.19	*0.04*	5.1	0.29	0.15	0.0005
La/Yb [d]	268	214	179	288	190	94	761	
La/Nb	12.4	10.7	1.2	0.7	11.0	4.8	46.7	
La/Rb	200	10.4	3.5	3.2	50.9	14.9	30.5	
Nb/U	12.1	5.9	14.4	35.6	29.1	10.1	3.7	
Zr/Eu	8.6	98.0	142	75.6	2.5	21.2	30.0	
Sr* (Sr/$\sqrt{}$(Pr×Nd)	5.9	29.6	59.4	32.9	1.6	17.1	12.9	

Table S-3 Sr-Nd-Sm-Pb isotope compositions of the HDFs in the analysed diamonds. [a] The amount of Sr (in ng) in the analysed samples normalised to the weight of the ablated material of each diamond – $Sr_{(analyzed\ sample)}$. [b] The amount of Sr in total procedural blank (TPB; in pg) – $Sr_{(TPB)}$. [c] Percent by weight of TPB = $Sr_{(average\ TPB)}/Sr_{(analyzed\ sample)}$. The same applies to Nd, Sm and Pb data. [b] Calculated initial values for a maximum possible emplacement age of 550 Ma; the value for diamond 502 was calculated using measured Rb value below LOD = 3 × $\sigma_{(TPB)}$. [e] $^{147}Sm/^{144}Nd$ calculated from the Sm and Nd isotope dilution data following equation: $^{147}Sm/^{144}Nd = (Sm/Nd) \times [0.531628 + 0.142556 \times {}^{143}Nd/^{144}Nd]$; the ratio for diamond 503 (red italics) calculated from ICPMS data as it was not measured for Sm by TIMS. Empty cell - not measured. Sr, Nd and Pb data for diamond 509 is from Weiss *et al.* (2022b); '509C' is the preferred duplicate of 509 for the present study as it has the smallest contribution of TPB on the isotopic composition of the measured samples (see Table 2 of Weiss *et al*., 2022b).

Diamond	502	503	505	508	509	515	516	TPB I	TPB II
Sr (ng) [a]	7.21	5.26	11.26	4.98	12.15	7.11	8.01	373 [b]	382
TPB % [c]	5 %	7 %	3 %	8 %	3 %	5 %	5 %		
$^{87}Sr/^{86}Sr$	0.71340	0.70571	0.70464	0.70438	0.70580	0.70741	0.70763		
2 sd	0.00003	0.00002	0.00002	0.00001	0.00003	0.00002	0.00001		
$^{87}Sr/^{86}Sr_{(550\ Ma)}$ [d]	*0.71332*	0.70512	0.70414	0.70338	0.70512	0.70687	0.70694		
Nd (ng)	1.87	0.32	0.37	0.30	15.02	0.77	0.96	4.8	7.9
TPB %	<1 %	2 %	2 %	2 %	<<1 %	<1 %	<1 %		
$^{143}Nd/^{144}Nd$	0.511774	0.512109	0.512628	0.512590	0.511914	0.512099	0.512296		
2 sd	0.000027	0.000151	0.000102	0.000122	0.000015	0.000043	0.000043		
$^{143}Nd/^{144}Nd_{(550\ Ma)}$	0.511424	0.511767	0.512387	0.512321	0.511588	0.511795	0.512036		
Sm (ng)	0.30		0.04	0.04	2.25	0.11	0.11	0.64	1.3
TPB %	<1 %		2 %	3 %	<<1 %	<1 %	<1 %		
$^{147}Sm/^{144}Nd$ [e]	0.0969	*0.0950*	0.0670	0.0748	0.0905	0.0844	0.0721		
2 sd	0.0001		0.0002	0.0002	0.0001	0.0001	0.0001		
Pb (ng)	3.32	0.57	13.2	0.45	3.15		26.4	225	239
TPB %	7 %	40 %	2 %	52 %	7 %		<1 %		
$^{206}Pb/^{204}Pb$	18.149	18.368	17.516	18.575	17.620		18.032		
2 sd	0.003	0.007	0.002	0.007	0.039		0.003		
$^{206}Pb/^{204}Pb_{(550\ Ma)}$	18.087		17.494		17.504		18.023		
$^{207}Pb/^{204}Pb$	15.680	15.646	15.580	15.632	15.531		15.611		
2 sd	0.003	0.006	0.002	0.006	0.033		0.003		
$^{207}Pb/^{204}Pb_{(550\ Ma)}$	15.676		15.579		15.525		15.610		
$^{208}Pb/^{204}Pb$	38.412	38.221	37.424	38.240	37.569		37.811		
2 sd	0.008	0.016	0.006	0.017	0.098		0.010		
$^{208}Pb/^{204}Pb_{(550\ Ma)}$	38.338		37.401		37.531		37.803		

Supplementary Figures

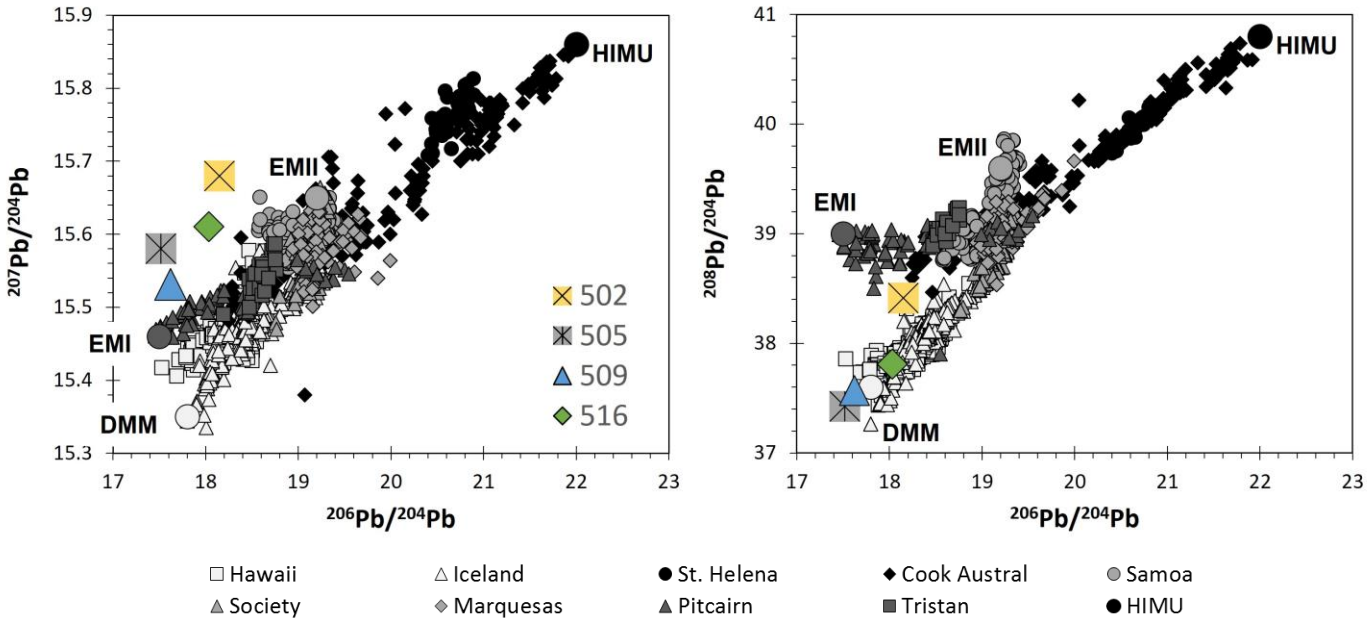

Figure S-1 Lead isotope ratio diagrams of HDFs in the studied diamonds (large coloured symbols). Mantle end-member components (large shaded circles), DMM – depleted mid-ocean ridge basalt (MORB) mantle, HIMU – high U/Pb (μ) mantle, and EMI and EMII – enriched mantle 1 and 2, are from Hart *et al.* (1992) and the isotopic variations for Hawaii, Iceland, St.Helena, Cook Austral, Samoa, Society, Marquesas, Pitcairn and Tristan (small shaded data points) are from the compilation of Stracke (2012).

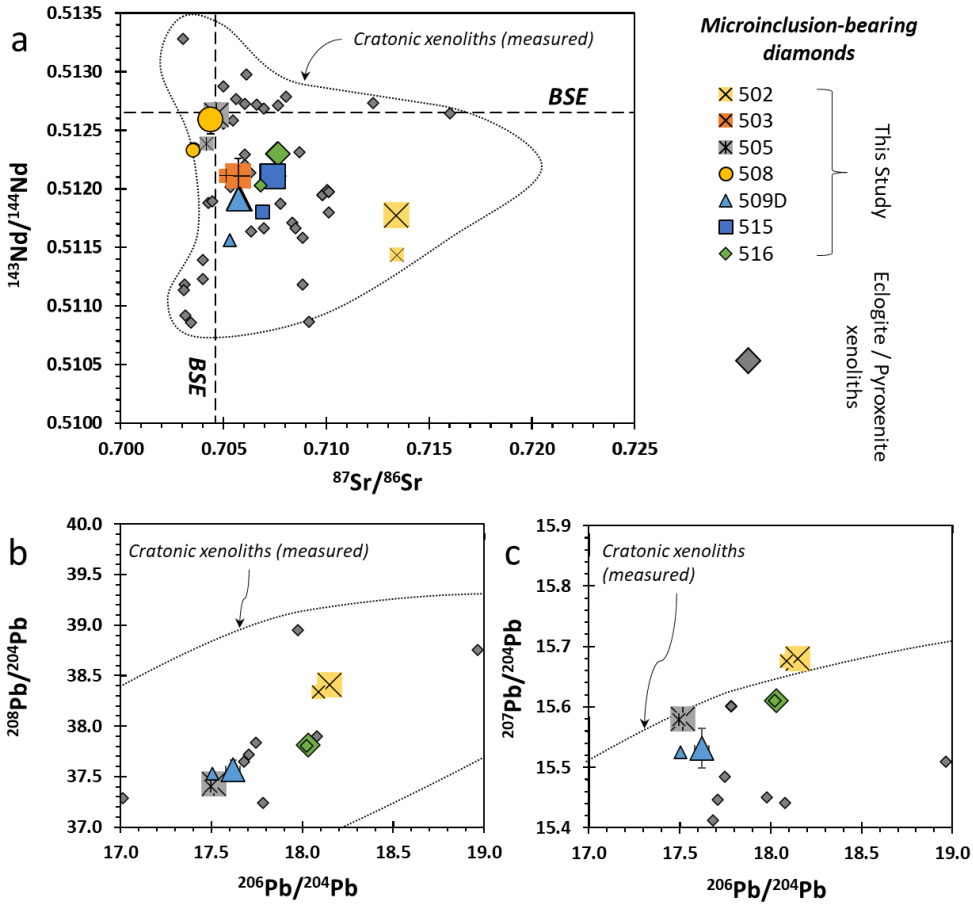

Figure S-2 Sr-Nd-Pb isotope compositions of HDF microinclusions in fibrous diamonds. **(a)** $^{143}Nd/^{144}Nd$ *vs.* $^{87}Sr/^{86}Sr$. Measured values (large coloured symbols) and initial ratios corrected for a maximum possible emplacement age of 550 Ma (small coloured symbols) are presented. The cratonic continental lithosphere isotopic compositional range, as determined based on whole rock xenolith data (dotted white area, based on the PetDB database; http://www.earthchem.org/petdb) of which eclogite and pyroxenite lithologies are highlighted (gray diamond data points), and BSE (Zindler and Hart, 1986) are presented for comparison. **(b)** $^{208}Pb/^{204}Pb$ *vs.* $^{206}Pb/^{204}Pb$; symbols and areas as in (a). **(c)** $^{207}Pb/^{204}Pb$ *vs.* $^{206}Pb/^{204}Pb$; symbols and areas as in (a).

Supplementary Information References

Agashev, A., Pokhilenko, N., McDonald, J., Takazawa, E., Vavilov, M., Sobolev, N., Watanabe, T. (2001) A unique kimberlite–carbonatite primary association in the Snap Lake dyke system, Slave Craton: evidence from geochemical and isotopic studies. *The Slave-Kaapvaal Workshop, Ext. Abstr. Vol. Merrickville, Canada, unpaged*.

Creaser, R.A., Grütter, H., Carlson, J., Crawford, B. (2004) Macrocrystal phlogopite Rb–Sr dates for the Ekati property kimberlites, Slave Province, Canada: evidence for multiple intrusive episodes in the Paleocene and Eocene. *Lithos* 76, 399-414. https://doi.org/10.1016/j.lithos.2004.03.039

Currie, L.A. (1968) Limits for qualitative detection and quantitative determination. Application to radiochemistry. *Analytical Chemistry* 40, 586-593. https://doi.org/10.1021/ac60259a007

Graham, I., Burgess, J., Bryan, D., Ravenscroft, P., Thomas, E., Doyle, B., Hopkins, R., Armstrong, K. (1999) Exploration history and geology of the Diavik kimberlites, Lac de Gras, Northwest Territories, Canada. *Proceedings of the VIIth International Kimberlite Conference, Cape Town 1, 262-279*

Hart, S.R., Hauri, E.H., Oschmann, L.A., Whitehead, J.A. (1992) Mantle Plumes and Entrainment – isotopic evidence. *Science* 256, 517-520. https://doi.org/10.1126/science.256.5056.517

Heaman, L.M., Creaser, R.A., Cookenboo, H.O. (2002) Extreme enrichment of high field strength elements in Jericho eclogite xenoliths: A cryptic record of Paleoproterozoic subduction, partial melting, and metasomatism beneath the Slave craton, Canada. *Geology* 30, 507-510. https://doi.org/10.1130/0091-7613(2002)030<0507:EEOHFS>2.0.CO;2

Heaman, L.M., Kjarsgaard, B.A., Creaser, R.A. (2004) The temporal evolution of North American kimberlites. *Lithos* 76, 377-397. https://doi.org/10.1016/j.lithos.2004.03.047

Howell, D., O'Neill, C.J., Grant, K.J., Griffin, W.L., Pearson, N.J., O'Reilly, S.Y. (2012) μ-FTIR mapping: Distribution of impurities in different types of diamond growth. *Diamond and Related Materials* 29, 29-36. https://doi.org/10.1016/j.diamond.2012.06.003

Howell, D., Weiss, Y., Smit, K.V., Loudin, L., Nestola, F. (2017) DiaMap: new applications for processing IR spectra of fluid-rich diamonds and mapping diamonds containing isolated nitrogen (Type Ib) and boron (Type IIb). *International Kimberlite Conference: Extended Abstracts* 11. https://doi.org/10.29173/ikc3831

Jablon, B.M., Navon, O. (2016) Most diamonds were created equal. *Earth and Planetary Science Letters* 443, 41-47. https://doi.org/10.1016/j.epsl.2016.03.013

Januszczak, N., Seller, M., Kurszlaukis, S., Murphy, C., Delgaty, J., Tappe, S., Ali, K., Zhu, J., Ellemers, P. (2013) A multidisciplinary approach to the Attawapiskat kimberlite field, Canada: accelerating the discovery-to-production pipeline. *Proceedings of 10th International Kimberlite Conference, Springer, 157–171*. https://doi.org/10.1007/978-81-322-1173-0_11

Kempe, Y., Weiss, Y., Chinn, I., Navon, O. (2021) Multiple metasomatic diamond-forming events in a cooling lithosphere beneath Voorspoed, South Africa. *Lithos*, 106285. https://doi.org/10.1016/j.lithos.2021.106285

Klaver, M., Smeets, R.J., Koornneef, J.M., Davies, G.R., Vroon, P.Z. (2016) Pb isotope analysis of ng size samples by TIMS equipped with a 10^{13} Ω resistor using a ^{207}Pb–^{204}Pb double spike. *Journal of Analytical Atomic Spectrometry* 31, 171-178. https://doi.org/10.1039/C5JA00130G

Koornneef, J.M., Bouman, C., Schwieters, J.B., Davies, G.R. (2014) Measurement of small ion beams by thermal ionisation mass spectrometry using new 10^{13}Ohm resistors. *Analytica Chimica Acta* 819, 49-55. https://doi.org/10.1016/j.aca.2014.02.007

Koornneef, J.M., Nikogosian, I., van Bergen, M.J., Smeets, R., Bouman, C., Davies, G.R. (2015) TIMS analysis of Sr and Nd isotopes in melt inclusions from Italian potassium-rich lavas using prototype 10^{13}Ω amplifiers. *Chemical Geology* 397, 14-23. https://doi.org/10.1016/j.chemgeo.2015.01.005

Lockhart, G., Grütter, H., Carlson, J. (2003) Temporal and geomagnetic relationship of Ekati economic kimberlites. *International Kimberlite Conference: Extended Abstracts*. https://doi.org/10.29173/ikc3185

Stracke, A. (2012) Earth's heterogeneous mantle: A product of convection-driven interaction between crust and mantle. *Chemical Geology* 330, 274-299. https://doi.org/10.1016/j.chemgeo.2012.08.007

Thirlwall, M. (2002) Multicollector ICP-MS analysis of Pb isotopes using a ^{207}Pb-^{204}Pb double spike demonstrates up to 400 ppm/amu systematic errors in Tl-normalization. *Chemical Geology* 184, 255-279. https://doi.org/10.1016/S0009-2541(01)00365-5

Weis, D., Kieffer, B., Maerschalk, C., Barling, J., de Jong, J., Williams, G.A., Hanano, D., Pretorius, W., Mattielli, N., Scoates, J.S., Goolaerts, A., Friedman, R.M., Mahoney, J.B. (2006) High-precision isotopic characterization of USGS reference materials by TIMS and MC-ICP-MS. *Geochemistry, Geophysics, Geosystems* 7. https://doi.org/10.1029/2006GC001283

Weiss, Y., Czas, J., Navon, O. (2022a) Fluid inclusions in fibrous diamonds. *Reviews in Mineralogy and Geochemistry* 88, 475-532. https://doi.org/10.2138/rmg.2022.88.09

Weiss, Y., Jockusch, S., Koornneef, J.M., Elazar, O., Davies, G.R. (2022b) Laser ablation of 'diamonds-in-water' for trace element and isotopic composition analysis. *Journal of Analytical Atomic Spectrometry*. https://doi.org/10.1039/D2JA00088A

Zindler, A., Hart, S. (1986) Chemical geodynamics. *Annual Review of Earth and Planetary Sciences* 14, 493-571. https://doi.org/10.1146/annurev.ea.14.050186.002425